Weight Multispectral Reconstruction Strategy for Enhanced Reconstruction Accuracy and Stability With Cerenkov Luminescence Tomography

Hongbo Guo, Xiaowei He,* Muhan Liu, Zeyu Zhang, Zhenhua Hu,* and Jie Tian*

***Abstract*— Cerenkov luminescence tomography (CLT) provides a novel technique for 3-D noninvasive detection of radiopharmaceuticals in living subjects. However, because of the severe scattering of Cerenkov light, the reconstruction accuracy and stability of CLT is still unsatisfied. In this paper, a modified weight multispectral CLT (wmCLT) reconstruction strategy was developed which split the Cerenkov radiation spectrum into several sub-spectral bands and weighted the sub-spectral results to obtain the final result. To better evaluate the property of the wmCLT reconstruction strategy in terms of accuracy, stability and practicability, several numerical simulation experiments and *in vivo* experiments were conducted and the results obtained were compared with the traditional multispectral CLT (mCLT) and hybrid-spectral CLT (hCLT) reconstruction strategies. The numerical simulation results indicated that wmCLT strategy significantly improved the accuracy of Cerenkov source localization and intensity quantitation and exhibited good stability in suppressing noise in numerical simulation experiments. And the comparison of the results achieved from different *in vivo* experiments further indicated significant improvement of the wmCLT strategy in terms of the shape recovery of the bladder and the spatial resolution of imaging xenograft tumors. Overall the strategy reported here will facilitate the development of nuclear and optical molecular tomography in theoretical study.**

***Index Terms*— Cerenkov luminescence tomography, Weight multispectral reconstruction, inverse problem.**

Manuscript received November 27, 2016; revised January 20, 2017; accepted January 22, 2017. Date of publication February 2, 2017; date of current version June 1, 2017. This work was supported in part by the National Natural Science Foundation of China under Grant 81227901, Grant 61372046, Grant 81527805, Grant 61231004, Grant 61622117, Grant 11571012, Grant 81671759, and Grant 61302024, and in part by the National Key Research and Development Program of China under Grant 2016YFC0102600. *Asterisk indicates corresponding author.*

H. Guo is with the School of Information Sciences and Technology, Northwest University, Xi'an 710069, China, and also with the Key Laboratory of Molecular Imaging, Institute of Automation, Chinese Academy of Sciences, Beijing 100190, China.

*X. He is with the School of Information Sciences and Technology, Northwest University, Xi'an 710069, China (e-mail: hexw@nwu.edu.cn).

M. Liu is with the Engineering Research Center of Molecular and Neuro Imaging of Ministry of Education, Xidian University, Xian 710071, China, also with the School of Life Science and Technology, Xidian University, Xian 710071, China, and also with the Key Laboratory of Molecular Imaging, Institute of Automation, Chinese Academy of Sciences, Beijing 100190, China.

Z. Zhang is with the Key Laboratory of Molecular Imaging, Institute of Automation, Chinese Academy of Sciences, Beijing 100190, China, and also with the Beijing Key Laboratory of Molecular Imaging, Beijing 100190, China.

*Z. Hu and *J. Tian are with the Key Laboratory of Molecular Imaging, Institute of Automation, Chinese Academy of Sciences, Beijing 100190, China, also with the Beijing Key Laboratory of Molecular Imaging, Beijing 100190, China, and also with the State Key Laboratory of Management and Control for Complex Systems, Chinese Academy of Sciences, Beijing 100190, China (e-mail: zhenhua.hu@ia.ac.cn; tian@ieee.org).

Digital Object Identifier 10.1109/TMI.2017.2658661

I. Introduction

CERENKOV luminescence imaging (CLI) is a novel molecular optical imaging technique based on the detection of Cerenkov photons emitted from radionuclides decaying with particle (β^-, β^+, and α) emission [1]–[4]. In the past years, CLI has been extensively investigated to image the distribution of radioisotopes such as ^{18}F, ^{64}Cu, ^{68}Ga, ^{32}P, and ^{131}I by many research groups [5]–[8]. The most attractive characteristic of CLI is combining the superiorities of optical imaging and nuclear imaging [9], [10]. To some existing optical imaging techniques, such as fluorescence molecular imaging (FMI) and bioluminescence imaging (BLI), one of the major limitations is lacking available optical probes in clinical applications. In contrary, many radiopharmaceuticals have beeen approved by food and drug administration (FDA) and they can be used for rapid translation of CLI into clinical practice [3], [11]–[13]. However, CLI is a planar imaging technique which is surface-weighted and incapable of tomographically revealing the internal features of targeted tissues [14]. To overcome the shortcomings of CLI, Cerenkov luminescence tomography (CLT) has been developed to restore the 3D distribution of interior radioactive probes [15]–[17].

Like some other 3D optical tomography techniques, there is also an ill-posed issue for CLT because of the severe scattering of Cerenkov luminescence [17]–[20]. In order to enhance the accuracy, one effective strategy is to combine some prior knowledge into CLT reconstruction. Historically, the first CLT reconstruction was based on a homogeneous model i.e. the optical properties of every organ are homogeneous and uniform [15]. Utilizing the anatomical structure information and the optical properties of heterogeneous biological tissues, Hu et al. established a heterogeneous model to reduce extra systematic errors. And the heterogeneous reconstruction results showed a remarkable improvement in tumor localization [14]. Multispectral information-based algorithm as another commonly utilized strategy has been widely adopted to reduce the ill-posedness of inverse reconstruction. Basing on a set of 2D planar images acquired by using a number of narrow bandpass filters, Spinelli et al. developed a multispectral

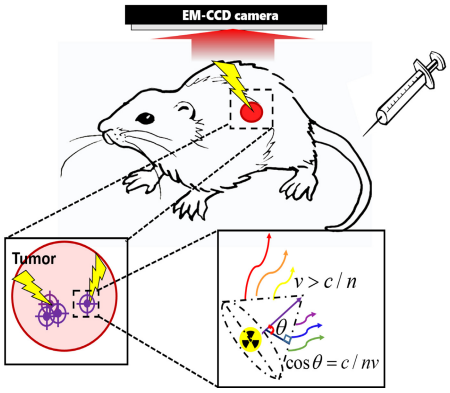

Fig. 1. The four stages in the whole photon propagation process.

CLT (mCLT) reconstruction method [16]. Compared with the results based on a single spectrum 675 − 775 nm, the mCLT can effectively improve the accuracy of the Cerenkov source location. Besides that, based on the spectrum feature of CR, an effective multispectral hybrid CLT (mhCLT) reconstruction method was established by Liu et al [21]. This new approach not only used the multispectral information, but also constructed a more accurate model to describe the propagation of CL photon. Expect these two general strategies, Hu et al. also presented a semi-quantitative hybrid spectral CLT (hCLT) reconstruction method [22]. This Cerenkov radiation spectral characteristic-based method can efficiently 3D noninvasive monitor ^{131}I uptake in the thyroid with both encouraging reconstruction results and less acquisition and image reconstruction time.

In this study, a modified weight multispectral CLT (wmCLT) reconstruction strategy was presented to improve the CLT reconstruction accuracy and stability. For wmCLT, the surface detected multispectral signals were split into several subspectral bands based on the CR spectral feature and the subspectral results were weighted to obtain the final result. To some extent, it avoids the multispectral data redundancy, the random error caused by a specific regulation parameter, and the possibility that some wavelengths dominate the objective function. To evaluate the performance of wmCLT strategy, numerical simulations and *in vivo* experiments were conducted. The results of wmCLT strategy have shown significant improvement in terms of accuracy, stability, and practicability.

II. Methodology

A. The wmCLT Strategy

As Fig. 1 shown, after the tail-vein injection of the radiopharmaceutical, the whole photon propagation process can be divided into four main stages. In stage 1, Cerenkov radiation is produced when the speed of particle v exceeds the speed of light in a medium (i.e $v > c/n$ where c and n are the speed of the light in vacuum and the refraction index of the medium, respectively). According to the Frank-Tamm theory, the light intensity is inversely proportional to the square of the wavelength $\frac{1}{\lambda^2}$ [23], [24]. In stage 2, due to the wavelength-dependent absorption and scattering of the tumor, the light yields would reduce. Only a small part of photons would pass through the tumor tissue and penetrate into the biological tissue. So the tumor spectral feature is no longer corresponding to the Frank and Tamm theory. In stage 3, CR signal intensity is further reduced by strong tissue attenuation and light scattering. And only the surface part of photons will be detected by the high sensitivity electron multiplied charge coupled device (EM-CCD) camera in stage 4.

In the second and third stage, the variation of the CR photons was abode by the radiative transfer equation (RTE). And RTE has mostly approximated as diffusion approximation equation when scattering effects within a region of interest are dominant over absorption effects. For 3D optical tomography, the diffusion approximation and the Robin-type boundary condition at a specific wavelength can be expressed [25]:

$$\begin{cases} -\nabla \cdot (D(r,\lambda)) + \mu_a(r,\lambda)\Phi(r,\lambda) = S(r,\lambda), (r \in \Omega) \\ \Phi(r,\lambda) + 2A(r,\lambda)D(r,\lambda)(v(r) \cdot D(r,\lambda)) = 0, (r \in \partial\Omega) \end{cases} \tag{1}$$

Where $\Phi(r,\lambda)$ denotes the luminescent flux density at position r, wavelength λ. $S(r,\lambda)$ provides the isotropic source energy distribution of the internal Cerenkov source, $D(r,\lambda)=1/3(\mu_a(r,\lambda) + \mu_s'(r,\lambda))$ is the diffusion coefficient with $\mu_a(r,\lambda)$ being the optical absorption coefficient and $\mu_s'(r,\lambda)$ is the reduced scattering coefficient. $A(r,\lambda)$ is the boundary mismatch factor accounting for different refractive indices across the boundary $\partial\Omega$, $v(r)$ denotes the unit outer normal. With the framework of finite element method (FEM), a relationship between the Cerenkov source distribution and the exiting partial luminescent flux fluence on the object boundary can be derived as [25]:

$$MX = \Phi \tag{2}$$

Where M denotes the optical transmission system matrix, Φ is the measured light flux at the boundary, and X denotes the radiopharmaceuticals distribution. Commonly the wavelength of photons did not change in light propagation process. So the surface-detected photons at specific wavelengths were emitted by the corresponding part of the Cerenkov source spectrum. Based on Eq. (2), we got another linear relation between the Cerenkov source and multispectral surface measurement for multispectral situation:

$$\begin{bmatrix} M_{\lambda 1}X_{\lambda 1} \\ M_{\lambda 2}X_{\lambda 2} \\ \cdots \\ M_{\lambda n}X_{\lambda n} \end{bmatrix} = \begin{bmatrix} \omega_{\lambda 1}M_{\lambda 1} \\ \omega_{\lambda 2}M_{\lambda 2} \\ \cdots \\ \omega_{\lambda n}M_{\lambda n} \end{bmatrix} X = \begin{bmatrix} \Phi_{\lambda 1} \\ \Phi_{\lambda 2} \\ \cdots \\ \Phi_{\lambda n} \end{bmatrix} \tag{3}$$

Where $M_{\lambda i}$ and $\Phi_{\lambda i}$ correspond to the system matrix and surface measurement in spectrum λi; $\omega_{\lambda 1}, \ldots, \omega_{\lambda n}$ are the multispectral weight of Cerenkov source. No direct solution exists, due to the ill-posedness of the inverse problem. Eq. (3) is instead usually solved as a regularized least squares problem with L1-norm non-negativity constraint. And for traditional multispectral CLT strategy, the solution can be obtained by solving the following equation:

$$X = \arg\min_X \frac{1}{2} \|\Xi X - \Phi\|_2^2 + \zeta \|X\|_1 \tag{4}$$

Algorithm 1 wmCLT Strategy

Initialization: In put the surface spectral measurement $\Phi_{\lambda i}$ and split the multispectral information into s sub-spectral bands.
Step 1: Calculate the spectral absorption coefficient $\mu_a(r,\lambda)$ and scattering coefficient $\mu_s'(r,\lambda)$.
Step 2: Determine the multispectral weight of CL source $\omega(\lambda n)$ and calculate the weighing coefficient of sub-spectral band $\mathrm{K}(\Gamma_i)$ by Eq. (5).
For $i = 1 : s$ do
Step 3: Construct system matrix $\Xi_{\Gamma i}$ by Eq. (1) and (3).
Step 4: using IVTCG to solve the inverse problem Eq. (4) and get the solution $X_{\Gamma i}$:
End
Step 5: Reconstruct the CL source by $X = \frac{1}{s}\sum_{i=1}^{s} X_{\Gamma i}/\mathrm{K}(\Gamma_i)$.

In which $\Xi = [\omega_{\lambda 1} M_{\lambda 1}, \ldots, \omega_{\lambda n} M_{\lambda n}]^T$, $\Phi = [\Phi_{\lambda 1}, \ldots, \Phi_{\lambda n}]^T$ and ζ is a regulation parameter, which is used to balance the relative weighing between the objective function term $\|\Xi X - \Phi\|_2^2$ and the penalty term $\|X\|_1$.

Considering the broad spectrum feature of Cerenkov light and the energy differences of the different spectral band, it's difficult to balance these two terms by using a fixed regulation parameter ζ. In previous research, we find that with the increasing of the surface measurements to a certain degree, some optical measurement data will be redundant and couldn't remit the ill-posedness of inverse problem [26]. So it is necessary to split the multispectral information into several sub-spectral bands and weight the sub-spectral results to obtain the final result. For wmCLT strategy, according to the spectral feature, the multispectral information is split into several sub-spectral bands Γ_i. And the final reconstruction results can be calculated by the weighted equation:

$$\begin{cases} X = \frac{1}{s}\sum_{i=1}^{s} X_{\Gamma i}/\mathrm{K}(\Gamma_i) \\ \mathrm{K}(\Gamma_i) = \dfrac{\int_{\Gamma_i^{min}}^{\Gamma_i^{max}} \omega(\lambda) d\lambda}{\int_0^{\infty} \omega(\lambda) d\lambda} \end{cases} \tag{5}$$

Where $X_{\Gamma i}$ is the reconstruction result of the $i-th$ sub-spectral band, which can be obtained by the traditional multispectral CLT strategy as Eq. (4) shown; $\mathrm{K}(\Gamma_i)$ denote the weighing coefficient of the $i-th$ sub-spectral band. Γ_i^{min} and Γ_i^{max} are the minimum and maximum of the wavelengths that belongs to the $i-th$ sub-spectral band. Herein, an effective L1 regularization reconstruction algorithm incomplete variables truncated conjugate gradient (IVTCG) method was introduced to solve Eq. (4) [27], [28].

So the wmCLT strategy using IVTCG can be summarized in Algorithm1.

B. Optical Properties and the Multispectral Weight

Absorption coefficient $\mu_a(r,\lambda)$ was approximated as a weighted sum of the absorption coefficients of the resident oxy-haemoglobin, deoxy-haemoglobin and water concentrations; Reduced scattering coefficient $\mu_s'(r,\lambda)$ was calculated by the empirical function: $\mu_s'(r,\lambda) = a \times \lambda^{-b}$, where a and b were constants controlling the spectral variation in each tissue [29]–[31]. In previous multispectral CLT reconstruction research, the multispectral weight of Cerenkov source $\omega(\lambda n)$ was generally substituted with $1/\lambda^2$ for approximation, without considering the influence of tumor absorption and scattering [16], [21]. However, the influence is inevitable, especially in some tumor tissue enriched with the severity of oxy-haemoglobin, deoxy-haemoglobin and water concentration [32]. In this paper, spatial location, optical properties, emission intensity and geometry shape, as four indicators of tumor tissue, were taken into consideration. As shown in Table 1, five different simulations (G1-G5) were conducted. And the corresponding $\omega(\lambda n)$ was calculated by Monte Carlo simulation based on Molecular Optical Simulation Environment (MOSE) [33].

TABLE I
THE SETUP OF TUMOR IN PRE-EXPERIMENTS FOR DETERMINING MULTISPECTRAL WEIGHT

Situation	Geometry shape	spatial location (mm)	optical properties (same as)	intensity (nw/sr)
G1	sphere	(16.0, 11.0, 16.5)	liver	100
G2	cylindrical	(16.0, 11.0, 16.5)	liver	100
G3	sphere	(22.8, 15.0, 26.0)	liver	100
G4	sphere	(16.0, 11.0, 16.5)	kidney	100
G5	sphere	(16.0, 11.0, 16.5)	liver	10

C. Spectral Attenuation Trends

In order to simulate the spectral attenuation trends, a common 3D digital mouse was utilized, which mainly include six organs: muscle, heart, lung, liver, stomach and kidney [34]. A cylindrical source of a $0.8mm$ radius and $1.6mm$ height was placed in the liver with center at $(16.0, 11.0, 16.5mm)$, meanwhile, $100nw/sr$ Cerenkov light was generated by radiopharmaceutical decay. Based on the gold standard Monte Carlo method, the luminescent flux density $\Phi(r,\lambda)$ at the position r was calculated. The spectral attenuation trends of Cerenkov photons at different wavelengths can be qualitatively described by absolute decay ration $\eta_a(\lambda_i(r))$ and relative decay ration $\eta_b(\lambda_i(r))$. Where $\eta_a(\lambda_i(r))$ is the ration of $\Phi(r,\lambda)$ and the previously set intensity of the Cerenkov light $(100nw/sr)$; $\eta_b(\lambda_i(r))$ is the ration of the $\Phi(r,\lambda)$ and the tumor emission photons at wavelength λ.

D. In vivo Experiments

All animals were purchased from the Department of Laboratory Animal Science, Peking University Health Science Centre (China). All animal experimental protocols were approved by the Institutional Animal Care and Use Committee, Chinese Academy of Sciences. And all the procedures were carried out in strict accordance with the appropriate institutional guidelines for animal research. Animal surgical and imaging procedures were performed under isoflurane gas anaesthesia (3% isoflurane air mixture), and all efforts were made to minimize suffering to mice. [18F]-Fluoro-2-deoxy-d-glucose

(^{18}F-FDG) was provided by the department of nuclear medicine, Chinese PLA General Hospital, Beijing, China. 4T1 mouse mammary tumor cells were cultured in Roswell Park Memorial Institute (RPMI) 1640 medium, completed by adding 10% fetal bovine serum and 1% penicllin-streptomycin, at 37°C in a humidified incubator in 5% CO2. The Balb/c nude mice were 6 weeks old and $20-25g$. Female mice were used for establishing 4T1 breast cancer xenografts.

In this study, two *in vivo* experiments, including the bladder reconstruction and *in vivo* imaging of xenograft tumors, were designed to verify the performance of the wmCLT strategy. In the bladder reconstruction, the Balb/c nude mice were injected with $800 \pm 50\mu ci$ ^{18}F-FDG through the tail vein and anesthetized with 2% isoflurane during the experiment. After $40min$, when circulation carried the ^{18}F-FDG to the bladder and tumor tissue, the surface CL image was acquired by an Andor EMCCD camera. In the acquisition process, the EMCCD camera was cooled to $-80°C$ to reduce the effects of thermal noise. Long exposure time ($5min$), high gain value (300), high shift speed ($12.9\mu secs$) and low speed readout rate (1MHz at 16-bit) were set up to increase the signal intensity and restrain the readout noise and the shift noise. Four optical filters (Semrock FF01-550/100-25, FF01-650/100-25, FF01-736/128-25, and FF01-855/210-25) were adopted to obtain the multispectral optical information. Then, the mice were taken to do a computed tomography (CT) scan using a micro-CT system to get the 3-D volume data. In the *in vivo* imaging of xenograft tumors, a double tumor-bearing mouse model was constructed by intravenous injection of highly metastatic 4T1 breast cancer cells. Approximately 1×10^6 4T1 breast cancer cells were injected into a BALB/c nude mouse. Tumors were allowed to grow for 2 weeks, and then the subsequent operations were similar to that of the bladder reconstruction experiment. Lastly, the positron emission tomography (PET) imaging and hematoxylin and eosin (H&E) stain were performed to verify the actual tumors area.

E. The Evaluation Index

Location error (LE), relative intensity error (RIE) and Dice coefficient were used to evaluate the reconstruction results. LE is the Euclidean distance between the centers of the reconstructed (x, y, z) and actual Cerenkov source (x_0, y_0, z_0): $LE = [(x-x_0)^2 + (y-y_0)^2 + (z-z_0)^2]^{1/2}$; RIE was adopted to evaluate the relative intensity deviation between the reconstructed Cerenkov source intensity I and the real source intensity I_0: $RIE = \frac{\|I-I_0\|}{I_0} \times 100\%$; For irregular-shaped organ with a specified volume, the classical Dice coefficient was adopted to measures the location accuracy of the reconstructed objects. Dice index was defined as: $Dice = \frac{2|X \cap Y|}{|X|+|Y|} \times 100\%$, where X is the reconstructed bladder region, Y is the true bladder region of every CT scans. It is obvious that Dice coefficient reflects the level of shape similarity between the reconstructed bladder and the actual bladder. And the Dice more close to 100%, the level of shape similarity is higher.

III. Results

In this section, the performance of the wmCLT strategy in terms of accuracy, stability and practicability were evaluated. This section is organized as follows: firstly, three important factors in the wmCLT strategy were described (including the optical properties, the multispectral weight, and spectral attenuation trends). Secondly, the reconstruction accuracy and stability were compared in numerical simulations. Lastly, the results of the bladder reconstruction and *in vivo* imaging of xenograft tumors were presented which further showed the superior practicability of the wmCLT strategy.

A. Optical Properties and the Multispectral Weight

The optical properties of biological tissue are the theory basis for multispectral signal-splitting in the process of the wmCLT strategy. The absorption coefficients and reduced scattering coefficients ($400-900nm$) for different organs were calculated and illustrated in Fig. 2 (a) and (b). As can be seen in the absorption spectrum, the Cerenkov spectrums can be split into three sub-spectral bands: (I) $400nm \leq \lambda < 650nm$, (II) $650nm \leq \lambda \leq 750nm$, (III) $750nm < \lambda \leq 900nm$. The absorption coefficient of the first sub-spectral band was much large than the other two sub-spectral band, which resulted in the most energy loss of Cerenkov photon energy.

The rationality of the multispectral weight of Cerenkov source $\omega(\lambda n)$ can affect the accuracy of the wmCLT reconstruction result. After Monte Carlo simulation, five groups of $\omega(\lambda n)$ were shown in Fig. 2(c). Although the values of multispectral weights have a little difference in each group, the five curves were very similar. The result indicated that the spatial location and geometry size had a very small impact on multispectral weights of Cerenkov source. Therefore in this study, the multispectral weight was approximated by averaging these five $\omega(\lambda n)$, as showed in Fig. 2 (d).

B. Spectral Attenuation Trends and Surface Photons Distribution

The spectral attenuation trends of Cerenkov light can be regard as the experimental evidence of multispectral signal-splitting. The 3D digital mouse and cylindrical Cerenkov source were illustrated in Fig. 3(a). After Monte Carlo simulation, the intensity of spectral lines of the unattenuated Cerenkov radiation and the source emission was illustrated in Fig. 3(b). The comparison spectral line indicated that source absorption and scattering resulted in the most loss of Cerenkov energy and less than 5% of the initial intensity would permeate through the biological tissue. That is, the real intensity of Cerenkov source was $4.4nw/sr$ in numerical experiments. In addition, absolute decay ration $\eta_a(\lambda_i(r))$ and relative decay ration $\eta_b(\lambda_i(r))$ were shown in Fig. 3(c) and Fig. 3(d). From these results, it appeared that with the increasing of the wavelength, the penetrability of the Cerenkov light with a certain energy was strong in many cases. From the surface photons distribution (Fig. 3(e)), we can found that the surface detected photons in the second sub-spectral bands ($\lambda \in [650, 750nm]$) was extremely high, next was the third sub-spectral bands

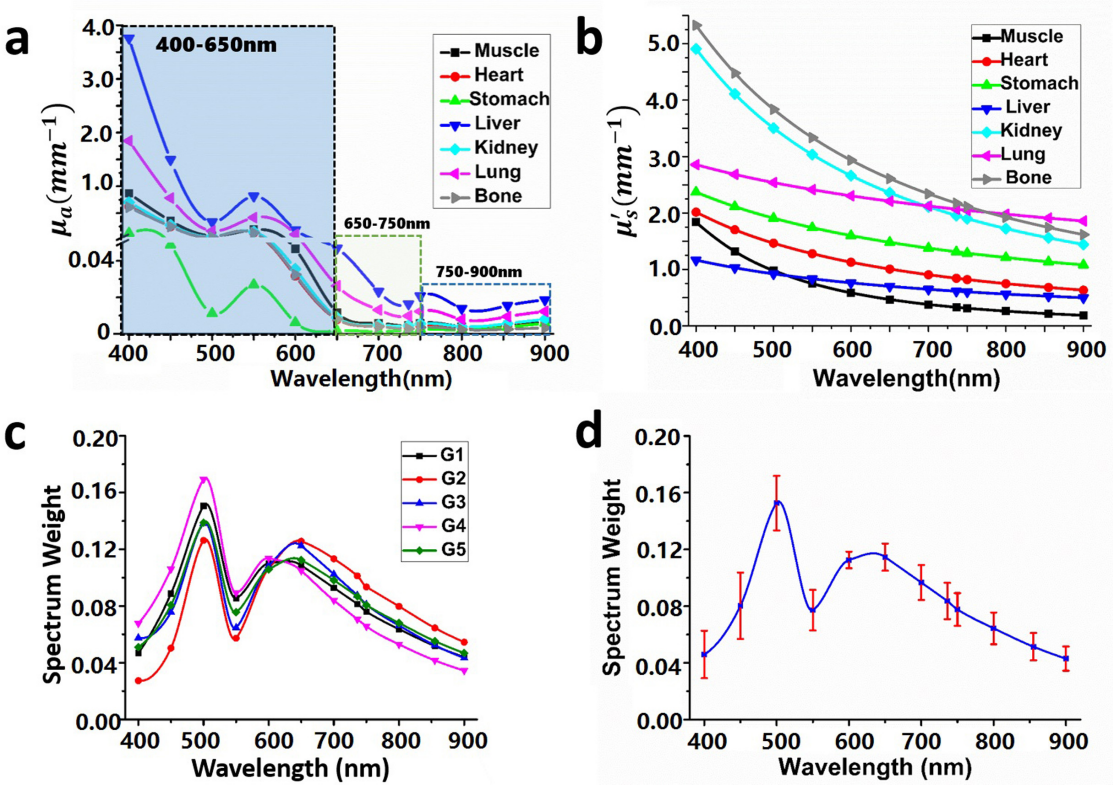

Fig. 2. The optical properties and the multispectral weight. (a) The absorption spectrum ($400-900nm$), which can be split into three sub-spectral bands: (I) $400nm \leq \lambda < 650nm$, (II) $650nm \leq \lambda \leq 750nm$, (III) $750nm < \lambda \leq 900nm$. (b) The reduced scattering coefficients ($400-900nm$). (c) The multispectral weight of Cerenkov source in five groups of pre-experiments. (d) The multispectral weight of Cerenkov source in this paper.

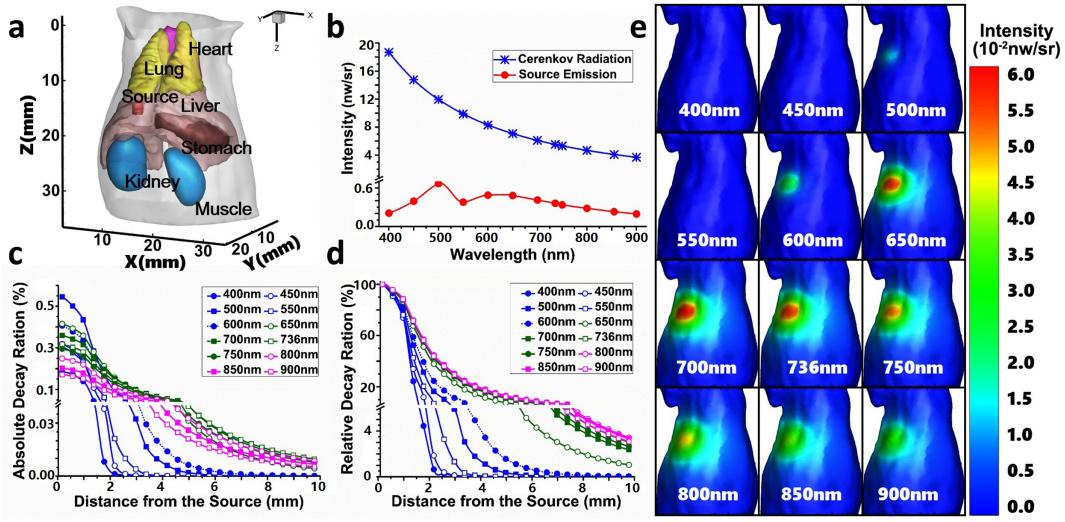

Fig. 3. The results of the spectral attenuation trends and surface photons distribution. (a) The digital mouse atlas of CT. (b) The spectral distribution of unattenuated Cerenkov radiation and source emission. (c) and (d) shows the absolute decay ration and the relative decay ration of CR intensity of different spectrums as the function of the penetration depth ($0-10mm$). (e) The surface photon distribution through different optical filters.

($\lambda \in (750, 900nm]$), which also confirmed the rationality of multispectral signal-splitting.

C. Accuracy Verification

For the inverse Cerenkov source reconstruction, the digital mouse model was divided into 15,318 tetrahedral elements and 3,085 nodes as Fig. 4(a) displayed. As shown in Fig. 3(e), nine spectra (500, 600, 650, 700, 736, 750, 800, 850, 900 nm) were employed to reconstruct the Cerenkov source. To evaluate the reconstruction performance, the traditional hCLT reconstruction, and mCLT reconstruction strategies were used to compare. Fig. 4 (b) showed the inverse reconstruction results of three reconstruction methods. In 3D view, the red cylindrical and the green area represented the real Cerenkov source and

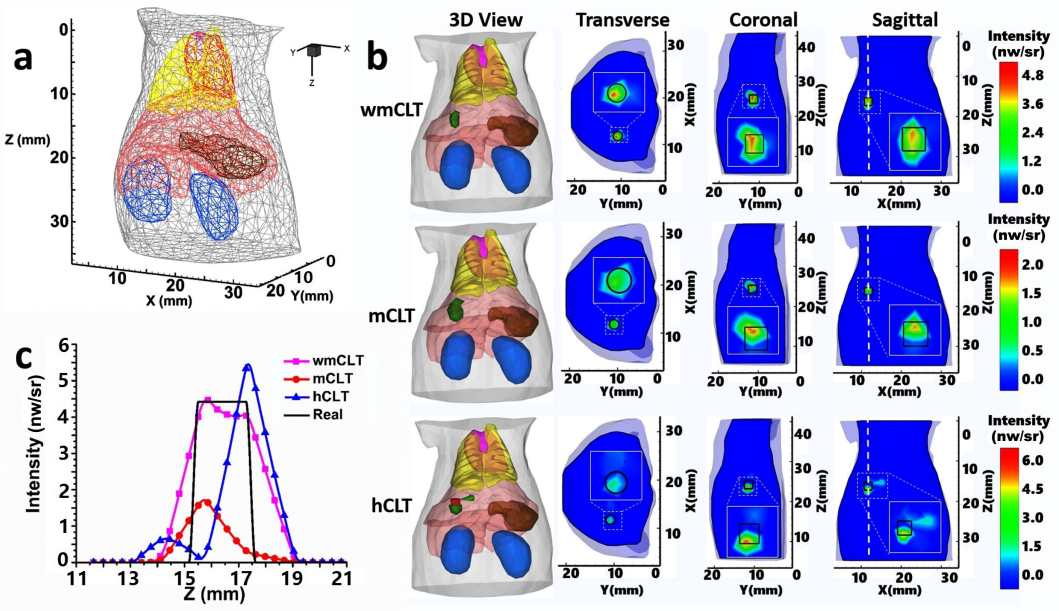

Fig. 4. The reconstruction results of the accuracy verification experiment. (a) the inverse reconstruction mesh. (b) the 3D view, transverse view, coronal view and sagittal view of weight multispectral CLT (wmCLT) reconstruction, multispectral CLT (mCLT) reconstruction and hybrid-spectral CLT (hCLT) reconstruction, respectively. (c) the intensity distribution of the reconstruction results along the z-axis of actual Cerenkov source center (i.e. the white dotted line in sagittal views).

TABLE II
QUANTITATIVE RESULTS FOR THE THREE CLT RECONSTRUCTION STRATEGIES IN NUMERICAL SIMULATIONS

Strategy	Position center (mm)	Intensity (nw/sr)	Location error (mm)	Relative intensity error
wmCLT	(11.6, 11.0, 16.5)	5.04	0.30	14.6%
mCLT	(11.6, 11.1, 15.7)	2.15	0.61	51.1%
hCLT	(11.8, 11.2, 17.3)	6.77	0.99	53.9%

the reconstructed Cerenkov source region, respectively. In the transverse, coronal and sagittal views, the local distribution information of the reconstructed tumor were also illustrated. Where the black edges denoted the true Cerenkov source margin and the color areas represented the reconstructed Cerenkov source area. Through the center of the real Cerenkov source and along the z-axis (i.e. the white dotted line in sagittal views), the intensity distribution curves were also drawn in Fig. 4 (c). Where the black line denoted the real distribution; the pink line, the red line and the blue line represented the reconstructed distribution by wmCLT, mCLT, and hCLT, respectively. To analyze the results quantitatively, Table 2 summarizes the reconstructed Cerenkov source position center, reconstructed Cerenkov source intensity, location error, and relative intensity error. The real position center and intensity of Cerenkov source were $(16.0, 11.0, 16.5mm)$ and $4.4nw/sr$, respectively. From the results, it was found that the reconstruction result of wmCLT was the best with a location error of 0.30 mm, and a relative intensity error of 14.6%. The position deviation of mCLT and hCLT was mainly along the z-axis, with the location error of 0.61 mm and 0.99 mm respectively. The relative intensity error of hCLT and mCLT were 53.9% and 51.1%, respectively. The results of comparison illustrate that wmCLT could significantly improve the accuracy of Cerenkov source localization and intensity quantitation.

D. Stability Comparison

To compare the stability of the wmCLT strategy, 10% additive Gaussian noise was added to the surface measurements. For the three reconstruction methods, independent simulations ($n = 4$) were performed. Statistical data were expressed as mean $\pm$ SD (Standard Deviation). From the statistical results, it found that the wmCLT strategy contained minuscule fluctuation with a location error of 0.33 ± 0.04 mm and a relative intensity error of $16.4 \pm 3.3\%$. The location error of mCLT and hCLT were 0.69 ± 0.07 mm and 1.00 ± 0.12 mm and the corresponding relative intensity error were $47.96 \pm 3.90\%$ and $56.21 \pm 27.9\%$, respectively. The comparison results validated that the wmCLT exhibited extremely good stability in suppressing noise.

E. Bladder Reconstruction

In order to assess the practicability of wmCLT strategy, the first *in vivo* experiment was focused on bladder reconstruction for studying the ^{18}F-FDG distribution in the bladder. The bladder reconstruction results are shown in Fig. 5(a)-(c) were the results of the proposed wmCLT strategy, traditional mCLT strategy, and hCLT strategy, respectively. In each figure, the 3D maximum intensity projection view (M), coronal view (C), sagittal view (S) and the transversal view (T) were also displayed in subfigures. The actual bladder edge was extracted from the CT scans as the black curves shown in each subfigure of (C), (T) and (S). It was obvious that the reconstruction bladder region of wmCLT strategy was closer to the actual

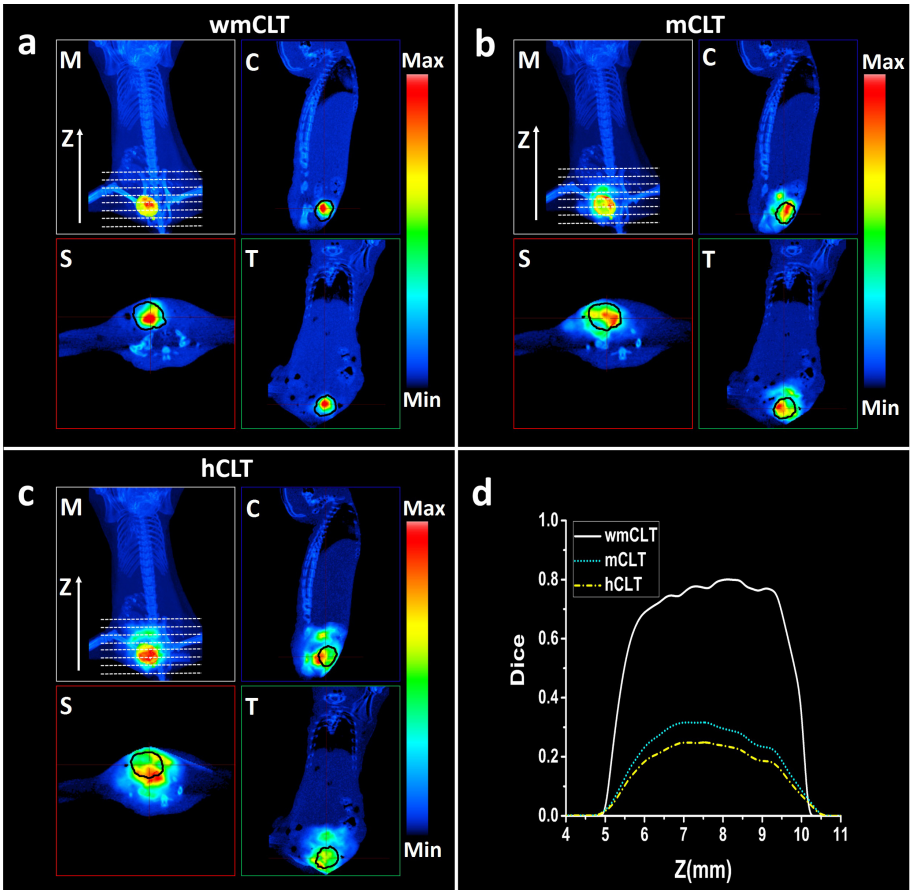

Fig. 5. The bladder reconstruction results. (a)-(c) are the results of our proposed wmCLT, traditional mCLT and hCLT respectively; in each figure, it also includes the 3D maximum intensity projection view (M), coronal view (C) and sagittal view (S) and the transversal view (T). (d) is the Dice index line of the fist 100 CT slices (as the white dotted lines in the 3D maximum intensity projection view (M) show), where the white solid line, blue short dotted line and the yellow short dash-dotted line represent the wmCLT, mCLT, and hCLT.

position than that of mCLT and hCLT strategy. According to the spatial distribution of actual bladder in CT scans, the Z-axis coordinates range of the actual bladder was $0 \leq Z \leq 12\ mm$. And the centroid position of the bladder confirmed by CT images was (41.1, 31.7, 7.8 mm). The Dice coefficient of the reconstructed bladder in the fist 100 CT slices (as the white dotted lines in the 3D maximum intensity projection view (M) show) were calculated as Fig. 5(d) illustrated. In Fig. 5(d), the white solid line, blue short dotted line and the yellow short dash-dotted line represented the Dice index of the wmCLT, mCLT, and hCLT, respectively. It is evident that wmCLT strategy has a high level of shape similarity with the level of similarity over 75%. The level of similarity was about 3 to 4 times more than that of mCLT and hCLT strategy. Lastly, the quantitative comparison of the results was listed in Table 3. In terms of bladder location, the location error of wmCLT, mCLT and hCLT were 0.93, 2.74 and 1.42mm, respectively. On the whole, our results indicated that the wmCLT strategy has a conspicuous improvement in bladder reconstruction in terms of the shape recovery and location accuracy.

TABLE III
QUANTITATIVE RESULTS FOR THE THREE CLT RECONSTRUCTION STRATEGIES IN BLADDER RECONSTRUCTION

Strategy	Real bladder centroid (mm)	Reconstructed bladder center (mm)	Location error (mm)
wmCLT	(41.1, 31.7 ,7.8)	(41.2, 32.5, 8.3)	0.93
mCLT	(41.1, 31.7 ,7.8)	(40.1, 31.7, 8.8)	1.42
hCLT	(41.1, 31.7, 7.8)	(39.9, 34.2, 7.6)	2.74

F. In vivo Imaging of Xenograft Tumors

Tumor detection, as one of the most common biological applications for CLT, has been widely studied in *in vivo* research. *In vivo* imaging of xenograft tumors, as the second *in vivo* experiment, was performed to testify the practicability of the wmCLT strategy. Observed through the CT slices, two tumors with the diameter of about 4.2 mm and 5.4 mm were in the abdomen of the mice. And the actual tumor centers were (46.64, 38.48, 22.31 mm) and (46.71, 38.08, 26.71 mm) with a center-to-center separation of 4.52 mm. The 3D imaging results of the wmCLT, mCLT and hCLT were shown given in Fig. 6(a)-(c), where T1 and T2 represented actual tumors detected by CT. For wmCLT strategy, the bladder and two tumors were clearly reconstructed. And the reconstructed tumor centers were (47.15, 39.03, 22.17 mm) and (47.82, 38.58, 26.47 mm) with the location deviation of 0.76 mm and 1.24 mm. For traditional mCLT strategy, only the

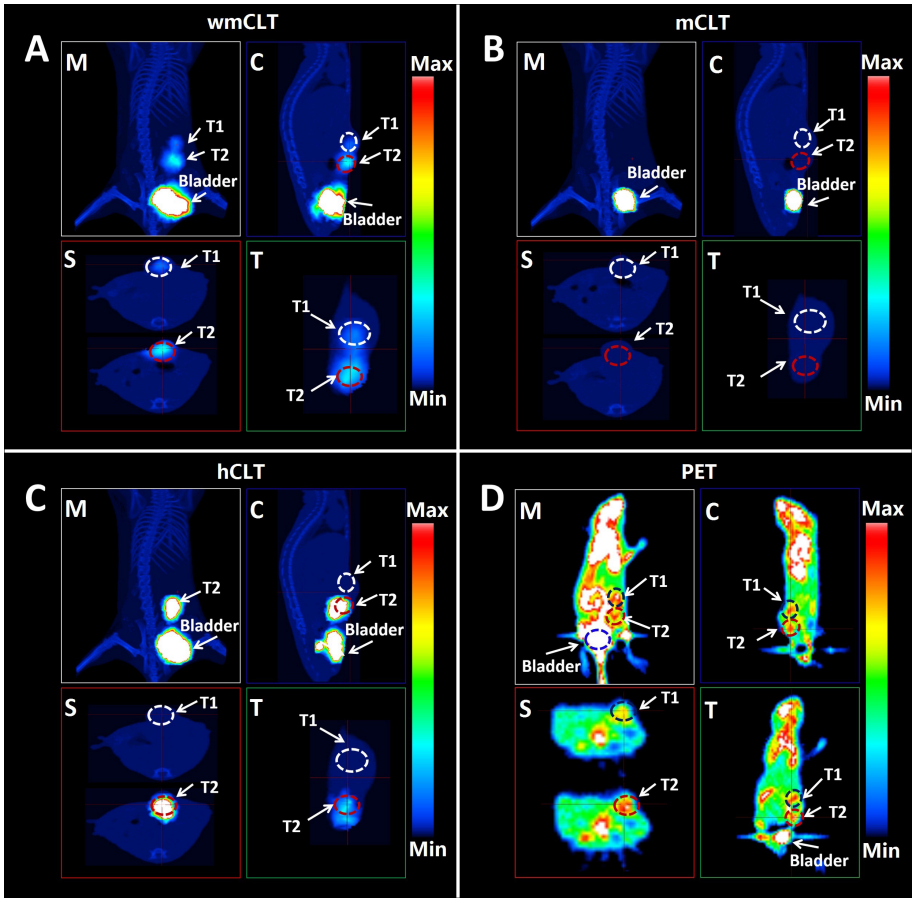

Fig. 6. The 3D detection results of xenograft tumors. (a)-(d) are the results of our proposed wmCLT, traditional mCLT, hCLT, and PET respectively; In each figure, it also includes the 3D maximum intensity projection view (M), coronal view (C) and sagittal view (S) and the transversal view (T).

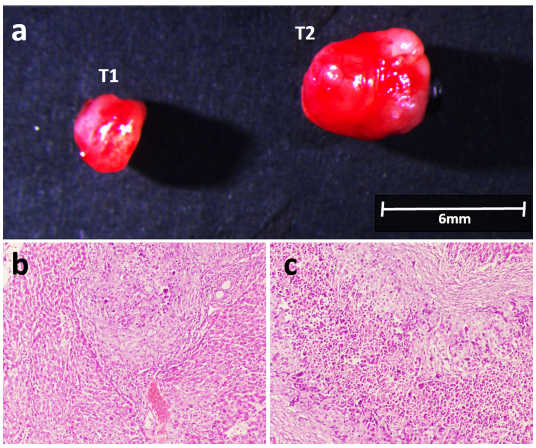

Fig. 7. The photograph and the H&E microscopy of the two tumors after dissection. (a) The photograph of the two tumors after dissection. (b) H&E result of tissue from T1. (c) H&E result of tissue from T2.

bladder was successful reconstructed. The two tumors did not detect. For traditional hCLT strategy, except for the bladder, only the tumor T2 was reconstructed, concentrating in the peripheral areas deeper inside the body with the coordinate of (47.82, 41.36, 21.70 mm). To quantitatively compare of PET and wmCLI strategy, PET imaging was performed at the indicated times as shown in Fig. 6(d). The figure illustrated that the high glucose metabolism and clearance areas, such as heart, bladder, liver and two tumors etc., which all showed a good functional imaging characteristic. Although the mouse body posture of the PET imaging was different from the CT imaging, the tumors reconstruction could still be reasonably compared. Comparison results indicated that wmCLT-based images were comparable with the corresponding PET images. Besides, the wmCLT strategy clearly revealed higher spatial resolution and signal to noise ratio than PET for superficial tumors. Lastly, Fig. 7 illustrated the photograph and the H&E staining images of the two tumors after dissection. These data clearly demonstrated that wmCLT strategy enables xenograft tumors detection with a satisfactory spatial resolution.

IV. Conclusion and Discussion

CLT has been used to reconstruct 3D distribution of radioactive probes inside living animals. However, the ill-posed of the inverse problem usually results in the reconstruction being non-robust. In this paper, we propose a wmCLT reconstruction strategy to improve the quality of reconstruction results. Experimental results demonstrate that the wmCLT strategy is more accuracy, stability and superior practicability than traditional mCLT and hCLT reconstruction strategies.

It should be pointed out that the key to the wmCLT strategy is the split-and-weight technique based on the CR spectral

feature. The split-and-weight technique is that the surface detected multispectral Cerenkov signals are split into several sub-spectral bands and the sub-spectral results are weighted to obtain the final result. To some extent, it avoids the multispectral data redundancy, the random error caused by a specific regulation parameter, and the possibility that some wavelengths dominate the objective function due to the smaller values of the absorption coefficient.

In addition, in wmCLT reconstruction, the optical properties, the multispectral weight, and spectral attenuation trends are three important elements that affect the accuracy of the reconstruction result. On one hand, the optical properties as a vital priority information is used to construct the optical transmission system matrix. On the other hand, the biological tissue optical properties is the theory basis for multispectral signal-splitting in the process of the wmCLT strategy. As illustrated in Fig. 2(a) and (b), the Cerenkov spectrums can be split into three sub-spectral bands: (I) $400nm \leq \lambda < 650nm$, (II) $650nm \leq \lambda \leq 750nm$, (III) $750nm < \lambda \leq 900nm$. The rationality of the multispectral signal-splitting was also confirmed by the spectral attenuation trends of Cerenkov light (Fig. 3(c) and (d)). We can conclude through comparative research that the first sub-spectral band (i.e. the ultraviolet and blue spectrum) has high absorption in biological tissues and limited penetration depth. While the second and third sub-spectral bands (i.e. the first near-infrared window) can penetrate biological tissues more efficiently. Thus, it is an important research subject to shifting the Cerenkov light from blue to red and near-infrared [11], [35].

The rationality of the multispectral weight of Cerenkov source $\omega(\lambda n)$ would affect the accuracy of the wmCLT reconstruction result. In order to determine multispectral weight $\omega(\lambda n)$, the whole photon propagation process is divided into four stages. As Fig. 3(b) shows, the tumor emission multispectral is no longer corresponding to Frank and Tamm theory because of tumor absorption and scattering. As a result, it is unreasonable that $\omega(\lambda n)$ is inversely proportional to the square of the wavelength $(1/\lambda^2)$. Fortunately, from the results of five multispectral weight pre-experiments as shown in Fig. 2(c), we can find that $\omega(\lambda n)$ is little affected by the difference of tumor spatial location and geometry size. Thus, the multispectral weight can be approximated by averaging these five $\omega(\lambda n)$, as showed in Fig. 2(d).

In numerical simulations, the accuracy and stability were evaluated. Compared with the traditional mCLT and hCLT strategy, wmCLT strategy can significantly improve the accuracy of Cerenkov source localization and intensity quantitation with the location error of 0.30 mm, and a relative intensity error of 14.6% (seen in Fig. 4 and Table 1). When 10% additive Gaussian noise was added to the surface measurements, the location error and relative intensity error is $0.33 \pm 0.04mm$ and $16.4 \pm 3.3\%$, respectively. The results indicate the wmCLT exhibits extremely good stability in suppressing noise.

In *in vivo* experiments, including the bladder reconstruction and *in vivo* imaging of xenograft tumors, two important biological applications of CLT have been conducted to investigate the practicability of the wmCLT strategy. In Fig. 5 and Table 2, the reconstruction bladder region of wmCLT strategy is very close to the actual bladder (location error, $0.93mm$, and level of shape similarity, 75%). While the comparison strategies are less effective with much image artifacts and location deviation. In Fig. 6, two xenograft tumors were clearly reconstructed only by the wmCLT strategy with the location deviation of $0.76mm$ and $1.24mm$. And the reconstructed images are comparable with corresponding PET, with a higher spatial resolution and signal to noise ratio. These *in vivo* results show that the wmCLT strategy has a conspicuous improvement in terms of the shape recovery of the bladder and the spatial resolution of xenograft tumors detection. It should be noticed that we didn't conduct an accurate quantitative research about the ^{18}F-FDG uptake in the *in vivo* experiments. Future work is about the quantitative research of CLT reconstruction by adopting the double-integrating-spheres system and some other quantitative strategies. Besides that, we will consider to build an optical reconstruction system that integrates the wmCLT strategy and some traditional reconstruction methods for some non-computer professionals.

In conclusion, a modified wmCLT strategy was presented which has a better performance in terms of accuracy, stability, and practicability. We believe that this strategy will further benefit various preclinical applications of CLT and facilitate the development of nuclear and optical molecular tomography in theoretical study.

REFERENCES

[1] A. Ruggiero, J. P. Holland, J. S. Lewis, and J. Grimm, "Cerenkov luminescence imaging of medical isotopes," *J. Nucl. Med.*, vol. 51, no. 7, pp. 1123–1130, 2010.

[2] Y. Xu, E. Chang, H. Liu, H. Jiang, S. S. Gambhir, and Z. Cheng, "Proof-of-concept study of monitoring cancer drug therapy with Cerenkov luminescence imaging," *J. Nucl. Med.*, vol. 53, no. 2, pp. 312–317, 2012.

[3] P. T. Chin, M. M. Welling, S. C. Meskers, R. A. V. Olmos, H. Tanke, and F. W. van Leeuwen, "Optical imaging as an expansion of nuclear medicine: Cerenkov-based luminescence vs fluorescence-based luminescence," *Eur. J. Nucl. Med. Mol. Imag.*, vol. 40, no. 8, pp. 1283–1291, 2013.

[4] C. Qin *et al.*, "Tyrosinase as a multifunctional reporter gene for photoacoustic/MRI/PET triple modality molecular imaging," *Sci. Rep.*, vol. 3, no. 12, p. 1490, 2013.

[5] D. L. J. Thorek *et al.*, "Cerenkov imaging—A new modality for molecular imaging," *Amer. J. Nucl. Med. Mol. Imag.*, vol. 2, no. 2, pp. 163–173, 2012.

[6] A. E. Spinelli *et al.*, "First human Cerenkography," *J. Biomed. Opt.*, vol. 18, no. 2, p. 020502, 2013.

[7] F. Boschi and A. E. Spinelli, "Cerenkov luminescence imaging at a glance," *Current Mol. Imag.*, vol. 3, no. 2, pp. 106–117, 2014.

[8] B. Xu *et al.*, "Evaluation of ^{68}Ga-labeled MG7 antibody: A targeted probe for PET/CT imaging of gastric cancer," *Sci. Rep.*, vol. 5, p. 8626, Mar. 2015.

[9] S. B. Lee *et al.*, "Radionuclide-embedded gold nanoparticles for enhanced dendritic cell-based cancer immunotherapy, sensitive and quantitative tracking of dendritic cells with PET and Cerenkov luminescence," *NPG Asia Mater.*, vol. 8, no. 6, p. e281, 2016.

[10] Z. Hu *et al.*, "*In vivo* 3-dimensional radiopharmaceutical-excited fluorescence tomography," *J. Nucl. Med.*, vol. 58, no. 1, pp. 169–174, 2017.

[11] Z. Hu *et al.*, "*In vivo* nanoparticle-mediated radiopharmaceutical-excited fluorescence molecular imaging," *Nature Commun.*, vol. 6, Jun. 2015, Art. no. 7560.

[12] G. S. Mitchell, R. K. Gill, D. L. Boucher, C. Li, and S. R. Cherry, "*In vivo* Cerenkov luminescence imaging: A new tool for molecular imaging," *Philos. Trans. Roy. Soc. London A, Math. Phys. Eng. Sci.*, vol. 369, no. 1955, pp. 4605–4619, 2011.

[13] M. R. Grootendorst, M. Cariati, A. Kothari, D. S. Tuch, and A. Purushotham, "Cerenkov luminescence imaging (CLI) for image-guided cancer surgery," *Clin. Transl. Imag.*, vol. 4, no. 5, pp. 353–366, 2016.

[14] Z. Hu *et al.*, "Experimental Cerenkov luminescence tomography of the mouse model with SPECT imaging validation," *Opt. Exp.*, vol. 18, no. 24, pp. 24441–24450, 2010.
[15] C. Li, G. S. Mitchell, and S. R. Cherry, "Cerenkov luminescence tomography for small-animal imaging," *Opt. Lett.*, vol. 35, no. 7, pp. 1109–1111, 2010.
[16] A. E. Spinelli *et al.*, "Multispectral Cerenkov luminescence tomography for small animal optical imaging," *Opt. Exp.*, vol. 19, no. 13, pp. 12605–12618, 2011.
[17] X. Ding, K. Wang, B. Jie, Y. Luo, Z. Hu, and J. Tian, "Probability method for Cerenkov luminescence tomography based on conformance error minimization," *Biomed. Opt. Exp.*, vol. 5, no. 7, pp. 2091–2112, 2014.
[18] J. Zhong, J. Tian, X. Yang, and C. Qin, "Whole-body Cerenkov luminescence tomography with the finite element SP_3 method," *Ann. Biomed. Eng.*, vol. 39, no. 6, pp. 1728–1735, 2011.
[19] Z. Hu *et al.*, "Cerenkov luminescence tomography of aminopeptidase N (APN/CD13) expression in mice bearing HT1080 tumors," *Mol. Imag.*, vol. 12, no. 3, p. 7290, 2013.
[20] C. Leng and J. Tian, "Mathematical method in optical molecular imaging," *Sci. China Inf. Sci.*, vol. 58, no. 3, pp. 1–13, 2015.
[21] H. Liu *et al.*, "Multispectral hybrid Cerenkov luminescence tomography based on the finite element SPN method," *J. Biomed. Opt.*, vol. 20, no. 8, p. 086007, 2015.
[22] Z. Hu *et al.*, "Three-dimensional noninvasive monitoring iodine-131 uptake in the thyroid using a modified Cerenkov luminescence tomography approach," *PLoS ONE*, vol. 7, no. 5, p. e37623, 2012.
[23] G. B. Collins and V. G. Reiling, "Čerenkov radiation," *Phys. Rev.*, vol. 54, no. 7, p. 499, 1938.
[24] X. Ma, J. Wang, and Z. Cheng, "Cerenkov radiation: A multifunctional approach for biological sciences," *Frontiers Phys.*, vol. 2, p. 4, Feb. 2014.
[25] Y. Lv *et al.*, "A multilevel adaptive finite element algorithm for bioluminescence tomography," *Opt. Exp.*, vol. 14, no. 18, pp. 8211–8223, 2006.
[26] H. Guo, J. Yu, X. He, Y. Hou, F. Dong, and S. Zhang, "Improved sparse reconstruction for fluorescence molecular tomography with $L_{1/2}$ regularization," *Biomed. Opt. Exp.*, vol. 6, no. 5, pp. 1648–1664, 2015.
[27] X. Wang, F. Liu, L. C. Jiao, J. Wu, and J. Chen, "Incomplete variables truncated conjugate gradient method for signal reconstruction in compressed sensing," *Inf. Sci.*, vol. 288, pp. 387–411, Dec. 2014.
[28] X. He *et al.*, "Sparse reconstruction for quantitative bioluminescence tomography based on the incomplete variables truncated conjugate gradient method," *Opt. Exp.*, vol. 18, no. 24, pp. 24825–24841, 2010.
[29] G. Alexandrakis, F. R. Rannou, and A. F. Chatziioannou, "Tomographic bioluminescence imaging by use of a combined optical-PET (OPET) system: A computer simulation feasibility study," *Phys. Med. Biol.*, vol. 50, no. 17, p. 4225, 2005.
[30] W. F. Cheong, S. A. Prahl, and A. J. Welch, "A review of the optical properties of biological tissues," *IEEE J. Quantum Electron.*, vol. 26, no. 12, pp. 2166–2185, Dec. 1990.
[31] R. M. Pope and E. S. Fry, "Absorption spectrum (380–700 nm) of pure water. II. Integrating cavity measurements," *Appl. Opt.*, vol. 36, no. 33, pp. 8710–8723, 1997.
[32] D. Grosenick, "Photon counting in diffuse optical imaging," in *Advanced Photon Counting*. Cham, Switzerland: Springer, 2015, pp. 343–365.
[33] J. Tian, J. Liang, X. Chen, and X. Qu, "Molecular optical simulation environment," in *Molecular Imaging*. Berlin, Germany: Springer, 2013, pp. 15–46.
[34] B. Dogdas, D. Stout, A. F. Chatziioannou, and R. M. Leahy, "Digimouse: A 3D whole body mouse atlas from CT and cryosection data," *Phys. Med. Biol.*, vol. 52, no. 3, p. 577, 2007.
[35] A. L. Antaris *et al.*, "A small-molecule dye for NIR-II imaging," *Nature Mater.*, vol. 15, pp. 235–242, Nov. 2015.